Cellulose (2012) 19:1051–1063
DOI 10.1007/s10570-012-9727-z

ORIGINAL PAPER

Dynamic vapor sorption and thermoporometry to probe water in celluloses

Carlos Driemeier · Fernanda M. Mendes · Marcelo M. Oliveira

Received: 9 February 2012 / Accepted: 15 May 2012 / Published online: 25 May 2012

Abstract Dynamic vapor sorption and thermoporometry probe complementary dimensions of water interaction with cellulose. While sorption is primarily sensitive to the first hydration layers, thermoporometry is primarily sensitive to the nanometric water-filled pores. In this article, these analytical techniques are detailed and applied to model mesoporous materials and to a wide spectrum of celluloses. Correlations between techniques are explored. In dynamic vapor sorption, celluloses present a general characteristic time of desorption. On the other hand, they present highly variable characteristic times of sorption, indicating that material-specific properties may be inferred from sorption kinetics. Regarding thermoporometry, the thermodynamics of ice melting in irregular pore shapes is introduced. Moreover, in our thermoporometry analysis with differential scanning calorimeter, freezing temperature is extended to −70 °C, allowing pores smaller than a few nanometers to be measured. Nevertheless, several data corrections are required for accurate thermoporometry at this condition. Comparisons between techniques show that sorption hysteresis is positively correlated with wet porosity. The presented developments and results will guide future application of these techniques to probe water in celluloses.

Keywords Cellulose · Adsorption · Desorption · Cryoporometry · Hydration

C. Driemeier · F. M. Mendes · M. M. Oliveira
Laboratório Nacional de Ciência e Tecnologia do Bioetanol—CTBE, Caixa Postal 6170, Campinas, São Paulo 13083-970, Brazil

C. Driemeier (✉)
Rua Giuseppe Máximo Scolfaro, 10000, Pólo II de Alta Tecnologia de Campinas, Caixa Postal 6170, Campinas CEP 13083-970, Brazil
e-mail: carlos.driemeier@bioetanol.org.br

Introduction

Understanding cellulose-water interactions has technological as well as fundamental importance. From a technological perspective, water is ubiquitous, and cellulose is the material of many industries, including textile, pharmaceutical (as cellulose fillers), pulp, paper, and, in the foreseeable future, cellulosic biofuels. From a fundamental perspective, there is a rich phenomenology in cellulose-water interactions. In the molecular scale, water forms hydrogen bonds to cellulose hydrophilic sites. In the nanoscale, water fills interfibrillar and interlamellar pores (Stone and Scallan 1968). And from microscopic to macroscopic scales, there is directional cellulose hygroexpansion (Skaar 1988; Burgert and Fratzl 2009).

Nevertheless, in spite of cellulose importance and devoted research, understanding of cellulose

organization in the nanoscale, the so-called ultrastructure, is still very incomplete. For celluloses that retain their native cellulose I crystal structures (which are the focus of this work), cellulose forms aggregates of microfibrils containing highly-ordered (crystalline) and less-ordered structures (Henriksson and Lennholm 2009). Moreover, cellulose ultrastructure affects hydration, as monolayer water mass depends on cellulose crystallinity indexes; and hydration affects ultrastructure, as water-filled pores collapse upon drying (Mihranyan et al. 2004; Kocherbitov et al. 2008). Nevertheless, in addition to such general properties, one also needs analytical techniques able to accurately and precisely measure material-specific ultrastructural parameters.

In this scenario, dynamic vapor sorption (DVS) and thermoporometry by differential scanning calorimetry (TP-DSC) are two thermal analyses techniques that probe complementary dimensions of water interaction with cellulose. While DVS is primarily sensitive to the first hydration layers, TP-DSC is primarily sensitive to the nanometric water-filled pores. It is noteworthy that DVS and TP-DSC can be highly automated, reducing analytical cost and increasing throughput.

Water sorption analysis is a classical tool to probe the *equilibrium* moisture contents adsorbed in hydrophilic polymers (Skaar 1988). The added *dynamic* capabilities in DVS allow additional investigation of sorption kinetics (Kohler et al. 2006; Xie et al. 2011). Thermoporometry (also named cryoporometry or thermoporosimetry) is based on the temperature depression of ice-water phase change inside pores (Petrov and Furó 2009). In the calorimetric version of the technique, TP-DSC, pore volumes are derived from measured heat flows due to phase transitions (Landry 2005).

In this article theoretical aspects of TP-DSC are further developed and DVS and TP-DSC are applied to model systems and to a wide spectrum of celluloses. Derived insights will guide DVS and TP-DSC application to ultrastructural investigations of other cellulosic materials.

This article is organized as follows. "Theory" section provides a theoretical background for analysis of sorption isotherms. It also details pore volume, area, and diameter determination by TP-DSC, including novel developments and discussions about achievable accuracy. "Experimental" section describes materials and experimental procedures. "Results and discussion" presents and discusses results in model mesoporous materials ("Mesoporous models" section) and in celluloses. Results for celluloses cover kinetic analysis with DVS ("Desorption and sorption kinetics" section), equilibrium isotherms from DVS ("Desorption and sorption equilibrium" section), TP-DSC ("Thermoporometry" section), and correlations between DVS and TP-DSC ("Correlations between techniques" section). Finally, "Conclusion" draws the conclusions of this work.

Theory

Hailwood–Horrobin sorption model

Sorption isotherms can be described by several models based on equilibrium thermodynamics (Skaar 1988). One of these models was developed by Hailwood and Horrobin (1946) (HH model), providing a simple framework to fit experimental sorption isotherms. Our presentation of the HH model follows Skaar (1988). Three coefficients m_0, K_h, and K_d describe a sorption isotherm $m(h)$ through the following equations:

$$\frac{h}{m} = A + Bh - Ch^2 \tag{1A}$$

$$A = 1/[m_0 K_d (K_h + 1)] \tag{1B}$$

$$B = (K_h - 1)/[m_0 (K_h + 1)] \tag{1C}$$

$$C = K_h K_d / [m_o (K_h + 1)] \tag{1D}$$

In Eqs. 1A–1D, h is the relative humidity ($0 \leq h \leq 1$), m is the adsorbed water mass (per unit of dry mass) and A, B, and C are constants derived from fitting $h/m \times h$ with a second-order polynomial (see Eq. 1A). The HH model considers that m_0 is the water mass (per unit of dry mass) that saturates sorption sites at solid surfaces (monolayer coverage), which has been assumed to be related to cellulose crystallinity (Hailwood and Horrobin 1946). The equilibrium constant of this monolayer hydration is K_h. In addition to monolayer water, there is water dissolved in the solid and K_d is the equilibrium constant of this dissolution. The coefficients m_0, K_h, and K_d are calculated from A, B, and C by solving Eqs. 1B–1D.

Standard free energy changes ΔG_h and ΔG_d (referenced to liquid water) are calculated (in units of J/g) from K_h and K_d, respectively, through

$$\Delta G_{h,d} = -(RT/\mu) \cdot \ln\left(K_{h,d}\right), \quad (2)$$

where R is the gas constant (8.314 J K^{-1} mol^{-1}), T is the absolute temperature, and μ is water molar mass (18 g mol^{-1}). ΔG_h is negative ($K_h > 1$), reflecting hydrophilic cellulose surfaces, while ΔG_d is positive ($0 < K_d < 1$), reflecting matrix opposition to its volumetric expansion required to dissolve water.

Pore volume in thermoporometry

TP-DSC discriminates three types of water (Maloney et al. 1998; Luukkonen et al. 2001; Park et al. 2006): (1) *free water* (also termed unbound water); (2) *freezing bound water*; and (3) *non-freezing bound water* (NFW). *Free water* is indistinguishable from bulk water; it is not an intrinsic material property, since free water is the water excess added during sample preparation. Free water is measured from ice melting at 0 °C. *Freezing bound water* is confined by the cellulosic solid in a way that shifts the temperatures of ice-water phase transitions; it is measured from ice melting below 0 °C. *NFW* originates from a few water layers adjacent to surfaces, which do not freeze because water motion is dimensionally restricted. NFW is estimated from the difference between total sample water and total freezing water (free water and freezing bound water).

In this work, TP-DSC is performed with the strategy of step-by-step ice melting previously applied to celluloses (Maloney et al. 1998; Luukkonen et al. 2001; Park et al. 2006). After freezing the wet sample, N sequential heating steps are performed. The ice mass M_i molten in each heating step ($i = 2,\ldots, N-1$) is calculated by

$$M_i = \frac{Q_i - C_i \cdot \delta T_i}{q_i} \quad (3)$$

where q_i is the specific enthalpy of ice melting, Q_i is the measured heat, C_i is the sample heat capacity, and δT_i is the programmed temperature rise in heating step i. Q_i and q_i are defined to be positive. Any self-consistent set of units can be employed. To convert from ice mass to pore volume, M_i is divided by ice density $\rho_{ice} = 0.917$ g/cm^3. The first heating step ($i = 1$) is assumed to melt no ice ($M_1 = 0$), implying $C_1 = Q_1/\delta T_1$. Freezing bound water melts from steps $i = 2,\ldots, N-2$. Free water melts at 0 °C, during step $N-1$. The last step N is fully above 0 °C; it does not melt any ice and, as the first step, only serves the determination of sample heat capacity, $C_N = Q_N/\delta T_N$.

The specific enthalpy q_i is calculated by considering its dependence on temperature (Landry 2005),

$$q_i(\mathrm{J/g}) = 334 + 2.119 \cdot \overline{T_i}(^\circ\mathrm{C}) - 0.00783 \cdot \left[\overline{T_i}(^\circ\mathrm{C})\right]^2 \quad (4)$$

where $\overline{T_i}$ is the mean temperature of the heating step i. An exception is made for the step $N-1$, in which free ice melts at 0 °C and one simply uses $q_{N-1} = 334$ J/g. It is noteworthy that Brun et al. (1977), by including the effects of ice-water interface curvature, derived different temperature dependence for q_i (see Equation 13 of their article). For example, at −40 °C their equation leads to $q_i = 190.6$ J/g, which is 20 % below $q_i = 236.7$ J/g calculated by Eq. 4. Such q_i difference approaches zero as temperature approaches 0 °C. Nevertheless, these differences make clear that uncertainties in q_i become significant at low temperatures, affecting the accuracy of M_i calculated by Eq. 3.

Estimation of C_i considers that heat capacity of each phase is a function of temperature and that specific heat capacity changes when ice melts to water. Starting with $C_1 = Q_1/\delta T_1$, for $i = 2,\ldots, N-2$ one calculates

$$C_i = C_{i-1} + \Delta C_i^{water} + \Delta C_i^{ice} + \Delta C_i^{nt} \quad (5A)$$

$$\Delta C_i^{water} = c^{water} \cdot M_i \quad (5B)$$

$$\Delta C_i^{ice} = c_i^{ice} \cdot \sum_{j=i+1}^{N} M_j - c_{i-1}^{ice} \cdot \sum_{j=i}^{N} M_j \quad (5C)$$

$$\Delta C_i^{nt} = M^{nt} \cdot \frac{dc^{nt}}{dT}\left(\overline{T_i} - \overline{T_{i-1}}\right) \quad (5D)$$

In this equation set, ΔC_i^{water}, ΔC_i^{ice}, ΔC_i^{nt} are heat capacity changes due to water, ice, and non-transforming components of the sample, respectively. The specific heat capacity of water c^{water} is taken as 4.21 J/gK for all i, and in Eq. 5B c^{water} is multiplied by M_i to account for gains in water mass due to ice melting. The specific heat capacity of ice c^{ice} is a function of temperature and is calculated by

$$c_i^{ice}(\mathrm{J/gK}) = 2.111 - 0.00777 \cdot \overline{T_i}(^\circ\mathrm{C}), \quad (6)$$

which is a linear approximation to reference data (Lide 2006). Ice mass changes due to melting, and $\sum_{j=i+1}^{N} M_j$ is the ice mass remaining after heating step

i, where j is the index of summation. The non-transforming mass M^{nt} is given by

$$M^{nt} = M^{spl} - \sum_{j=1}^{N} M_j, \tag{7}$$

where M^{spl} is the wet sample mass and the summation is the total freezing water. Finally, dc^{nt}/dT is the temperature derivative of the specific heat capacity of the non-transforming sample component, which is estimated from dedicated measurements. As an exception, C_{N-1} is calculated as a weighted mean of C_{N-2} (calculated by Eqs. 5A–5D) and $C_N = Q_N/\delta T_N$.

Equations 3 and 5A–5D are coupled through C_i and M_i. This coupling is solved iteratively, using M_i from previous iteration to calculate C_i. Starting with $M_i = 0$ (except for M_{N-1}), a convergent numerical solution is achieved within four iterations.

TP-DSC results are presented as *cumulative* pore size distributions, expressed as freezing bound water per unit of sample dry mass M^{dry}. NFW, which is the difference between sample water ($M^{spl} - M^{dry}$) and total freezing water (ΣM_i), is also given per unit of M^{dry}. Determination of NFW is subject to significant uncertainties because it is the difference of two much larger quantities.

Pore area and diameter in thermoporometry

Following the thermodynamic development by Petrov and Furó (2009), there are two fundamental equations that describe the temperature depression ΔT of ice-water phase transitions inside pores:

$$\Delta T = -K_C \frac{S}{V} \tag{8A}$$

$$\Delta T = -K_C \frac{\partial S}{\partial V} \tag{8B}$$

S is the ice-water interface area, V is the volume of the ice phase, and K_c is a simple function of enthalpy and temperature of the bulk phase transition, liquid density, and ice-water interface energy. Equation 8A describes thermodynamic equilibrium, while Eq. 8B describes the removal of the energy barrier for melting. Petrov and Furó (2009) argued that, under special conditions, *freezing* is described by equilibrium (Eq. 8A), while *melting* is described by removal of the energy barrier (Eq. 8B). Indeed, pore geometries could be inferred from measured differences between ΔT of freezing and melting. The aforementioned special conditions include pores with diameter larger than $\approx$3 nm (in which ice melts above ≈ -40 °C) and simple pore geometries (sphere, cylinder, and slit).

Ice premelting in a more complex pore geometry (voids in a matrix of spheres) was described by Hansen-Goos and Wettlaufer (2010). One important consideration of their work was the liquid water pocket that forms at the contact between spheres. By increasing temperature, there is a *continuous* advance of the water pocket (a continuous recession of ice) associated with a continuous increase in the radius of curvature of the ice-water interface.

We further develop this idea by considering a hypothetical long pore with square cross-section (Fig. 1). We do not claim that squared pores are realistic in cellulose. Instead, squared pores are considered here only as a source of insights about melting near pore edges (absent in cylindrical or spherical pores). When temperature is low enough, ice fills the pore, except for the water layer at wall surface and the water pockets at vertices, where the ice-water interfaces have a finite radius of curvature. Considering a continuous increase in temperature, we propose a *first stage of melting* in which ice continuously recedes and the radius of curvature associated with pore edges continuously *increase*. In this first stage, indicated by arrows in Fig. 1, there is no barrier for ice recession. Ice melting is hence described by equilibrium (Eq. 8A). The *second stage of melting* would take place after ice reaches a cylindrical shape (dotted line in Fig. 1). Continuous ice recession is no longer possible because it requires the radius of curvature to *decrease*. Hence, further melting faces a barrier. When the rising temperature meets the condition for barrier removal (Eq. 8B), all remaining pore ice (the ice cylinder) melts in a single event.

Two fundamental lessons are learned from previous paragraphs. First, it is ice-water interface area S (not pore diameter) that is the natural variable associated with ΔT, as clear from Eqs. 8A and 8B. This is a mere consequence of thermoporometry being based on ice-water interface energies. Second, for complex pore geometries, which are expected in celluloses, there is interplay between the equilibrium (Eq. 8A) and barrier removal (Eq. 8B) conditions for ice melting. These two conditions are related to melting of pore *edges and cores*, respectively.

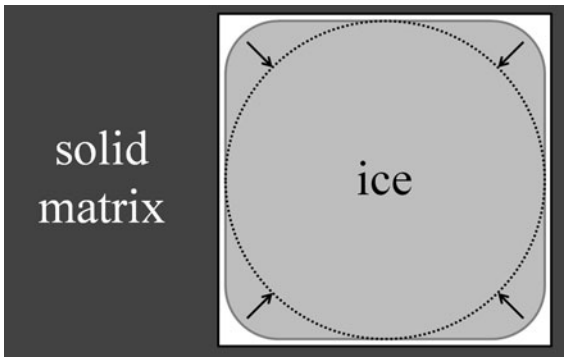

Fig. 1 Proposed two-stage ice melting in a long pore with square cross-section. The first stage (*arrows*) is the recession of ice near vertices, which proceeds through a continuous increase of radius of curvature. The second stage is the single-step melting of the ice cylinder (*dotted line*). Liquid water is represented in *white*

In spite of this interplay, only Eq. 8B is employed in the following development. This is the usual simplification, which is justifiable as an approximation, particularly for the higher temperatures that melt the core of pore volumes, as the cylinder of Fig. 1. In this context, the derivative in Eq. 8B can be integrated to estimate total pore area A

$$A = \int \frac{-\Delta T}{K_C \cdot \rho_{ice}} dM \tag{9}$$

where the differential solid volume dV was replaced by the differential solid mass dM divided by ice density ρ_{ice}. For TP-DSC performed with discrete heating steps, discretization of the integral is required.

Although pore surface is the natural variable of thermoporometry, it is still convenient to express porosity as a function of estimated pore diameters. Using Eq. 8B and assuming cylindrical pores of diameter x,

$$\frac{\partial S}{\partial V} = \frac{2}{x} \tag{10A}$$

$$x = -2 \cdot K_c / \Delta T. \tag{10B}$$

Equation 10B is a concise form of the Gibbs–Thomson equation commonly used in thermoporometry. In Petrov and Furó (2009) review, tabulated estimates for K_c vary within 21–53 nm K. In this article, we follow previous TP-DSC work on celluloses and use $K_c = 19.8$ nm K. This was the K_c used by Park et al. (2006) and is close to $K_c = 21.6$ nm K used by Luukkonen et al. (2001).

Experimental

Materials

Mesoporous silicas MCM-41 (643645) and MSU-H (643637) were acquired from Sigma-Aldrich (catalog code in parenthesis). These materials have approximately cylindrical pores of uniform diameters, which make them valuable porous models (Lowell et al. 2010). Nominal (provided by manufacturer) pore diameters are 2.3–2.7 and 7.1 nm, while nominal pore volumes are 0.98 and 0.91 cm^3/g, respectively. These nominal pore diameters and volumes were reproduced (within 10 %) in our lab using N_2 adsorption (not shown), which is a dry measurement technique.

The present study also analyzed a heterogeneous set of celluloses, which is a well suited set to discriminate general and material-specific properties. Several celluloses were acquired from Sigma-Aldrich: Fluka cellulose (22183), Sigmacell type 20 (S3504), Sigmacell type 50 (S5504), Avicel PH-101 (11365), Sigmacell type 101 (S6790), and α-cellulose (C8002). These samples are henceforth named Fluka, S20, S50, Avicel, S101, and Alpha, respectively. We also acquired two bleached eucalyptus kraft pulps, Celufloc 200, and Whatman #1 filter paper, henceforth named EkP1, EkP2, Floc, and FP, respectively. Finally, the set includes a sugarcane bagasse pulp produced in a mixture of acetic acid and hydrogen peroxide (courtesy of Dr. Juliano Bragatto), a eucalyptus pulp produced in subcritical CO_2-ethanol–water (courtesy of Dra. Maria Teresa Borges Pimenta), and a film of bacterial (Acetobacter) cellulose (courtesy of Dr. Hernane Barud, UNESP Araraquara). These samples are henceforth named BapP, EscP, and BC, respectively. All cellulose samples presented X-ray diffraction patterns of cellulose I (not shown) and were handled in laboratory atmosphere before conditioning for thermal analyses.

Vapor sorption

DVS was performed in a TA Q5000 SA instrument, which measures sample mass while controlling relative humidity h in sample chamber. This control is done through modulation between flows of dry N_2 ($h = 0$) and saturated water vapor ($h = 1$). Instrument calibration followed manufacturer recommendations. DVS analysis was done at 50 °C aiming at

accelerating sorption and desorption processes. Relative humidity was first set equal to 0.95, then 0.90, and then decreased in 0.10 steps until zero. It was then increased in the reverse order. Relative humidity was stepped every 60 min, except at $h = 0$, which was kept during 180 min to improve the definition of sample dry mass ($\approx$5 mg, except when stated otherwise).

Other researchers (Kohler et al. 2006; Xie et al. 2011) used variable intervals for h stepping. If intervals are long enough to approach equilibrium, we consider fixed intervals better because identical conditions are applied to all samples. Moreover, fixed intervals ease laboratory schedule because total analysis time is fixed.

Thermoporometry

TP-DSC was performed in a TA DSC-Q200 instrument with autosampler and RCS90 cooling unit. Instrument calibration followed manufacturer recommendations, using sapphire for baseline, and indium melting for cell constant and temperature calibrations. Temperature uncertainties were within ±0.03 °C near 0 °C, as inferred by testing isothermal melting of bulk ice. Referencing the temperature to the onset of ice melting (in a heating ramp) was avoided because of ice premelting (Dash et al. 2006) and thermal lagging (Landry 2005).

Cellulose samples were conditioned by immersion for $\approx$24 h in deionized water. Wet samples were then inserted in Tzero® aluminum pans that were immediately sealed with hermetic lids. Masses from the pan-lid set, empty and filled with the wet sample, were determined gravimetrically. The mass difference is sample wet mass M^{spl}. After the TP-DSC run, the lid was perforated and water evaporated at 105 °C during 2 h. The resulting sample dry mass M^{dry} was recorded. The difference $M^{spl} - M^{dry}$ is the water mass. Samples dry masses of 1–6 mg and water:solid ratios within 1–3:1 were typical. This sample mass variability is due to difficulty in precise handling of wet celluloses.

In each TP-DSC run, the sample was initially frozen to −70 °C and then $N = 18$ heating steps were performed sequentially. Each step was composed by a heating ramp (at 1 °C/min) and an equilibrating isotherm. Temperatures of isotherms were −70.0, −60.0, −50.0, −40.0, −30.0, −20.0, −15.0, −10.0, −6.0, −4.0, −2.0, −1.5, −1.1, −0.8, −0.5, −0.2, −0.1, 0.5, and 5.0 °C. Measured heat flows at the ends of isotherms were used to build a corrected heat-flow baseline, which assumed linear dependence on temperature between sequential isothermal ends. The major advantage of TP-DSC by step-by-step heating is its better baseline definition, which is crucial for samples with broad pore size distributions (as celluloses are). Heats Q'_i ($i = 1,\ldots, N$) were determined by time integration of heat flows (subtracted out of baseline). Corrected heats $Q_i = \kappa\ Q'_i$ were used in Eq. 3. The corrective factor ($\kappa \approx 1.03$) was derived by additional calibration that required $q = 334$ J/g for measurements of bulk ice melting (samples of pure deionized water). Moreover, for celluloses $dc^{nt}/dT = 0.0067$ J g^{-1} K^{-2} (see Eq. 5D) was estimated from measurements with samples containing 10–20 % water.

Results and discussion

Mesoporous models

A marked feature of raw DVS data from MCM-41 and MSU-H (Fig. 2a) is the presence of a relatively fast mass loss (gain) during desorption (sorption), changing water content between a high level (0.6–0.7 g/g) and a low level (0.1–0.2 g/g). This transition corresponds to capillary evaporation (condensation) and it is better observed in Fig. 2b, which shows water contents as a function of relative humidity. It is clear that the material with larger pores (MSU-H, red squares) has the transitions at higher relative humidities than the material with smaller pores (MCM-41, blue circles). This relation with pore size, as well as presence of hysteresis (as in Fig. 2b), is typical of capillary evaporation–condensation (Lowell et al. 2010). We must note, however, that the 60 min intervals were not enough to approach equilibrium during these steps of capillary transitions. In addition, both model materials presented the same behavior for $h \leq 0.4$, corresponding to water desorption and adsorption at pore surfaces. There is no evidence of water binding inside silica matrices, indicating that silica wet and dry porosities are equal.

Raw TP-DSC thermograms (Fig. 2c) present notable endothermic peaks (*) that appear at higher temperature for MSU-H ($\approx$−15 °C, red) than for MCM-41 ($\approx$−40 °C blue), reflecting the larger pores of MSU-H. The analyzed TP-DSC data (average of

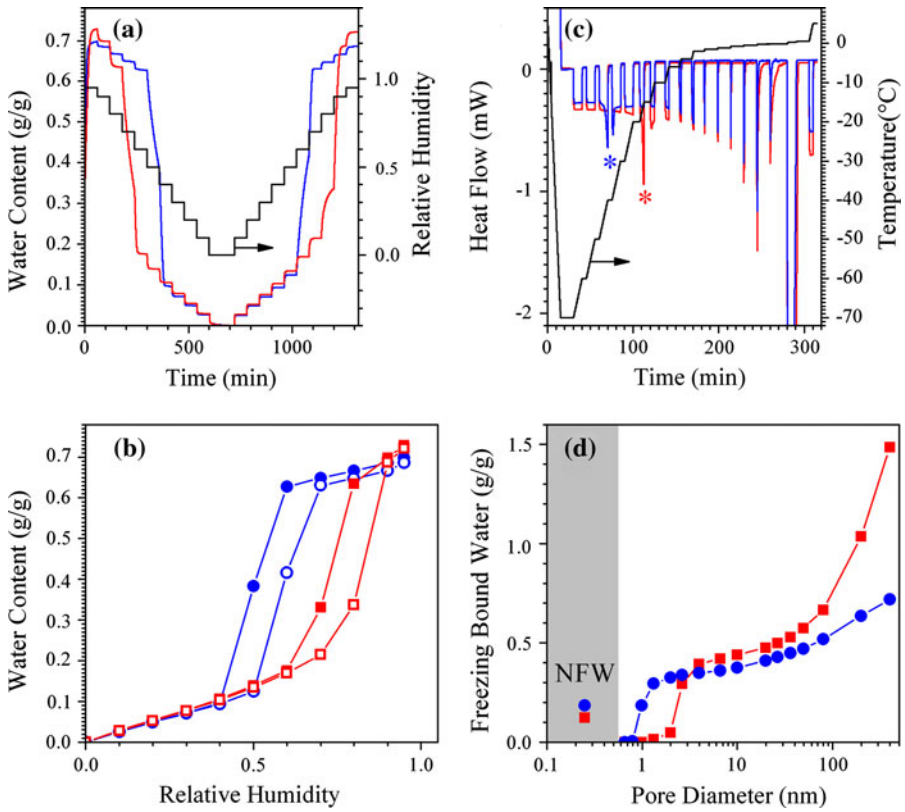

Fig. 2 Dynamic vapor sorption and thermoporometry applied to model mesoporous materials. **a** Raw dynamic vapor sorption data, with water contents expressed per unit of dry mass. **b** Desorption (*filled symbols*) and sorption (*empty symbols*) isotherms, in which water contents were taken from the end of relative humidity steps. **c** Raw differential scanning calorimetry thermograms with indication (*) of pore melting signals at ≈ -40 °C (*blue*) and ≈ -15 °C (*red*), corresponding to pores diameters of ≈ 1.0 and ≈ 2.6 nm, respectively. **d** Analyzed thermoporometry results, with points in the gray area showing contents of non-freezing water, NFW (g/g). Nominal pore diameters are 2.3–2.7 nm for MCM-41 (*blue lines* and *circles*) and 7.1 nm for MSU-H (*red lines* and *squares*). (Color figure online)

two measurements for each material) is shown in Fig. 2d, where the *y*-axis is the cumulative freezing bound water. The leading edges of the distributions are at ≈ 1.0 nm (MCM-41, blue circles) and ≈ 2.6 nm (MSU-H, red squares), corresponding to pore melting derived from the endothermic peaks (*) in Fig. 2c. Additional freezing bound water at pore diameters beyond a few nm (see Fig. 2d) likely corresponds to interparticle voids formed by wet sample sedimentation (MCM-41 and MSU-H are particulates) inside DSC pans.

A first lesson from model mesoporous systems is that both DVS and TP-DSC are sensitive to pores of a few nanometers. A second lesson is that pore diameters derived from TP-DSC are correct comparatively, but underestimated systematically (as compared to nominal pore diameters). Part of this underestimation is due to the NFW layer at pore surfaces, which reduces the diameter of the freezing volume; and part is due to uncertainties in K_C (see Eq. 10B and discussion thereafter). A third lesson is that pore volumes, as inferred from vapor saturation at ≈ 0.7 g/g (Fig. 2b), are significantly below nominal pore volumes of 0.98 and 0.91 cm^3/g (considering water density of 1.0 g/cm^3 for unit conversion). Such a difference may be due to uncertainty in nominal pore volumes or lower water density inside nanometric pores. Another meaningful comparison is between vapor saturation level in DVS (≈ 0.7 g/g, for both MCM-41 and MSU-H, as read in Fig. 2b) and bound water in TP-DSC (≈ 0.55 g/g, NFW plus freezing bound water just after leading edges of cumulative distributions, as read in Fig. 2d). The pore volume underestimation by TP-DSC very likely arises from q_i

(and C_i) estimates used in Eq. 3. Nevertheless, uncertainty in q_i becomes negligible for larger pores (in which ice melts closer to 0 °C).

Desorption and sorption kinetics

Our first attempt to analyze desorption and sorption kinetics was with the parallel exponential kinetics model, which was previously applied to DVS of celluloses (Kohler et al. 2006; Xie et al. 2011). This model fits mass as a function of time (within each relative humidity step) by two added exponentials ($A_1e^{-t/\tau 1} + A_2e^{-t/\tau 2}$). The two exponential terms represents the fast and the slow components of sorption kinetics. Although the achieved fits look good based on a R^2 criterion (as also mentioned in the aforementioned work) fit residuals (not shown) are clearly not random, indicating inadequate fitting function. In particular, the derived slow characteristic time significantly varies with the extension of the fitting interval. Therefore, the parallel exponential kinetics was abandoned and another approach was developed, which avoids assumption of any mathematical function.

Raw data of a DVS analysis of Avicel is shown in Fig. 3, with one relative humidity step (gray area) detailed in the inset. An initial fast mass change is observed in addition to a slower component that extends to the end of the step. The inset of Fig. 3 illustrates our procedure for obtaining kinetic parameters. The mass change in each step was normalized (from 0 to 1) and the times $t_{1/2}$, $t_{1/4}$, $t_{1/8}$, and $t_{1/16}$ were annotated. These are the times required to reach, respectively, 1/2, 3/4, 7/8, and 15/16 from the mass change of the step.

An initial analysis with variable Avicel dry masses (2, 5 and 10 mg) demonstrated that $t_{1/2}$ (which is a characteristic time of the fast kinetics) depends on sample mass (see Fig. 4, top). Hence, $t_{1/2}$ does not reliably inform about intrinsic material properties. The observed trend of longer $t_{1/2}$ for higher sample mass is consistent with fast kinetics limited by mass and/or heat flows, because more sample mass implies more water exchange required in each step. This effect of sample mass propagates to $t_{1/4}$, $t_{1/8}$ and $t_{1/16}$ with asymptotically decreasing magnitudes. Taking the difference $t_{1/16}$–$t_{1/8}$ (which is a characteristic time of the slow kinetics) results in negligible dependence with sample mass (see Fig. 4, bottom). Therefore, this characteristic time ($t_{1/16}$–$t_{1/8}$) is henceforth taken to represent vapor desorption and sorption kinetics.

For Avicel, $t_{1/16}$–$t_{1/8}$ is approximately constant among desorption steps, while there is substantial $t_{1/16}$–$t_{1/8}$ variation among sorption steps, with $t_{1/16}$–$t_{1/8}$ monotonically increasing with h (see Fig. 4, bottom). The observed $t_{1/16}$–$t_{1/8}$ variability (considering desorption and sorption) demonstrates that $t_{1/16}$–$t_{1/8}$ is not defined to be intrinsically constant; it is rather able to

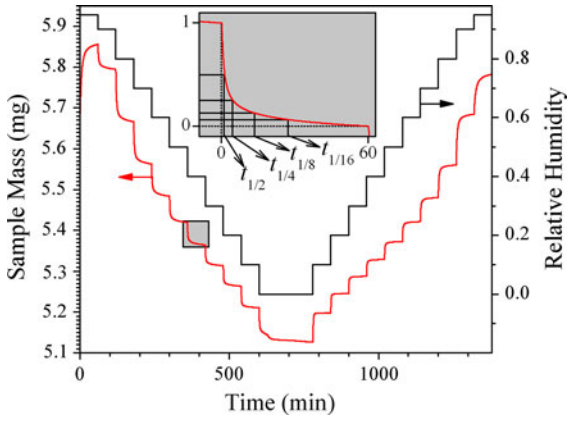

Fig. 3 Raw dynamic vapor sorption data from Avicel. The inset shows how characteristic times $t_{1/2}$, $t_{1/4}$, $t_{1/8}$, and $t_{1/16}$ were derived from normalized mass change in the marked (*gray area*) relative humidity step

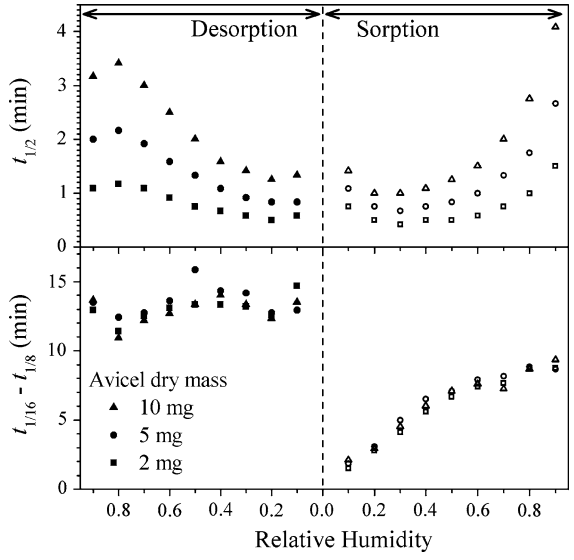

Fig. 4 Dynamic vapor sorption characteristic times from Avicel analyzed with different sample dry masses (2, 5 and 10 mg). The fast kinetics is represented by $t_{1/2}$ (*top*) and the slow, by $t_{1/16}$–$t_{1/8}$ (*bottom*)

represent kinetic variability. In particular, the rapid equilibration during low-h sorption steps is visible in the raw data of Fig. 3 and is coherently represented by low $t_{1/16}$–$t_{1/8}$ in Fig. 4.

Characteristic times ($t_{1/16}$–$t_{1/8}$) from the celluloses of this study are compared in Fig. 5. Since desorption $t_{1/16}$–$t_{1/8}$ do not appreciably depend on h, for each sample we took the eight $t_{1/16}$–$t_{1/8}$ desorption measurements in the interval $h = 0.1,\ldots, 0.8$ and calculated the mean and the standard deviation (shown in Fig. 5 as solid squares and bars, respectively). It is striking that all celluloses (except BC) presented very similar desorption characteristic times, with mean $t_{1/16}$–$t_{1/8}$ within 12.8 and 13.8 min, and standard deviations within 1.0 and 2.0 min. This general behavior indicates that desorption kinetics is governed by a phenomenon independent of cellulose structure.

Figure 5 also shows that sorption characteristic times are systematically below those from desorption, implying that sorption is comparatively faster. It is also noteworthy that $t_{1/16}$–$t_{1/8}$ behavior as a function of h varies; while for a few samples (e.g., Avicel) $t_{1/16}$–$t_{1/8}$ monotonically increases with h, for others (e.g., S101) $t_{1/16}$–$t_{1/8}$ is maximum at intermediate $h \approx 0.4$ (compare stars and triangles in Fig. 5). Moreover, 1σ precisions in sorption $t_{1/16}$–$t_{1/8}$ ($\sigma \approx 0.5$ min, as estimated from standard deviations in repeated measurements of selected samples) are very below observed variability among samples (Fig. 5). Thus, sorption kinetics provides material-specific structural information, but result interpretation is not yet clear.

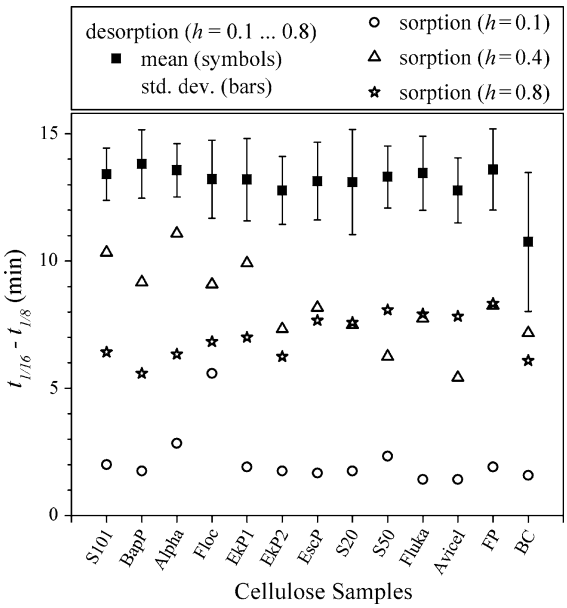

Fig. 5 Dynamic vapor sorption characteristic times ($t_{1/16}$–$t_{1/8}$) from the analyzed cellulose samples. Desorption times are shown as mean and standard deviation of eight measurements (relative humidity h between 0.1 and 0.8). Sorption times are shown for selected h (0.1, 0.4, and 0.8)

Desorption and sorption equilibrium

Analysis of desorption and sorption equilibrium isotherms were done with masses measured at the end of each relative humidity step (see Fig. 3). Actually, those are not strict equilibrium conditions; they are rather two approximations to equilibrium. The resulting desorption and sorption isotherms were fitted by the HH model (see "Hailwood–Horrobin sorption model" section). Only data at $h \leq 0.8$ was considered in the fits. This restriction is justified because $h = 0.80$ is the first desorption step reached by $\Delta h = 0.1$, which is the Δh applied to all other analyzed steps. In addition, fits are appreciably improved by avoiding data at $h > 0.80$.

Measured and fitted isotherms for two celluloses (Avicel and S101) are shown in Fig. 6, exemplifying observations made for all celluloses. Desorption and sorption isotherms are of type II (Lowell et al. 2010), and desorption isotherms are always above the

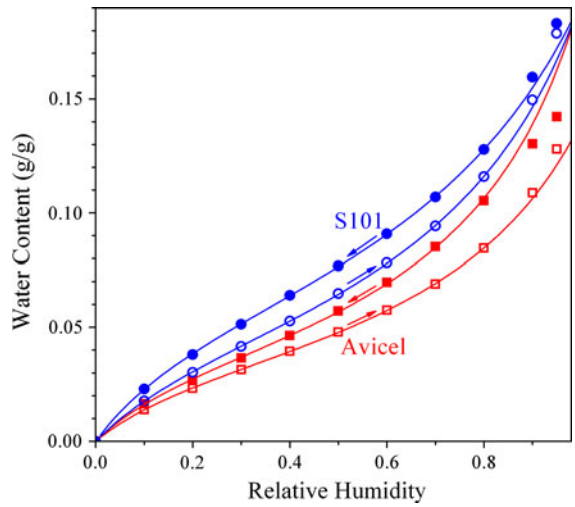

Fig. 6 Desorption (*solid symbols*) and sorption (*empty symbols*) isotherms from Avicel (*red squares*) and S101 (*blue circles*). Fits by the Hailwood-Horrobin model (*lines*) included data up to relative humidity of 0.8. (Color figure online)

corresponding sorption ones, which is the well known hysteresis. The HH fits precisely describe experimental data within the analyzed range ($h \leq 0.8$), but fit extrapolation to $h = 0.90$ and $h = 0.95$ appreciably deviates from measured points.

Derived HH-model parameters are shown in Fig. 7 for all cellulose samples, ordered from highest to lowest sorption m_0. (Note that the same sample order has been used in Fig. 5.) Precisions (1σ) in these HH-model parameters were estimated from standard deviations in repeated measurements of selected samples. They are lower than $\sigma m_0 \approx 0.0006$ g/g, $\sigma \Delta G_h \approx 8$ J/g, $\sigma \Delta G_d \approx 1$ J/g. Therefore, for all the HH model parameters there are significant differences among celluloses shown in Fig. 7.

Thermoporometry

In this work sample freezing temperatures went down to −70 °C, while previous TP-DSC analyses of celluloses were limited to −30 °C (Park et al. 2006) or −45 °C (Maloney et al. 1998; Luukkonen et al. 2001). As indicated by Eq. 10B, lower temperatures allow measurement of smaller pores. Using the same raw experimental data (from Avicel or S101), Fig. 8 demonstrates that a modified data analysis starting from −40 °C misses (more significantly for S101) the small (≈nm) pores that are evidenced by the standard analysis starting from −70 °C. These pores that became measurable at −70 °C have sizes compatible with interfibrillar voids.

An additional consequence of starting from lower temperatures is the enhanced importance of the C_i corrective terms (see Eq. 5A–5D), which were absent (or not explicit) in previous TP-DSC analysis of celluloses (Maloney et al. 1998; Luukkonen et al. 2001; Park et al. 2006). Regarding these corrections, Fig. 8 presents other modified data analyses in which (1) ΔC^{nt}, (2) $\Delta C^{water} + \Delta C^{ice}$, or (3) all ΔC (implying $C_i = C_1$) were neglected. These modified data analyses resulted in substantial porosity overestimation, demonstrating that the C_i corrective terms are crucial

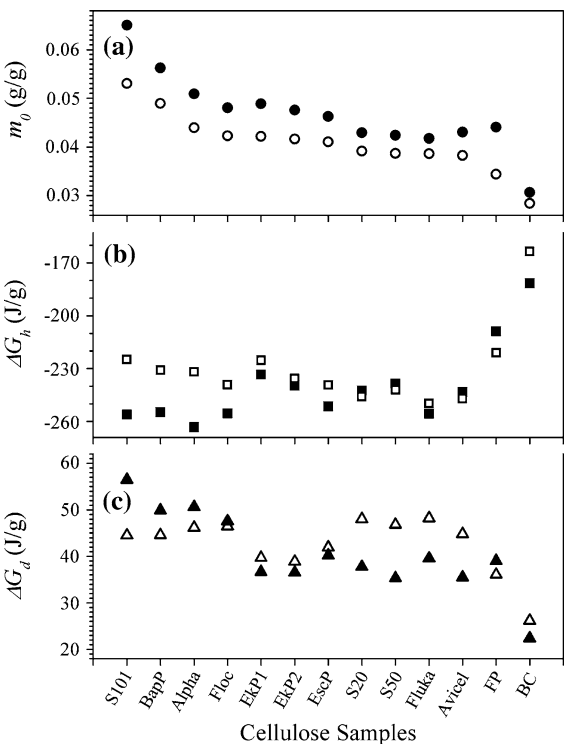

Fig. 7 Hailwood-Horrobin model parameters **a** m_0, **b** ΔG_h, and **c** ΔG_d for desorption (*solid symbols*) and sorption (*empty symbols*) isotherms from the different cellulose samples

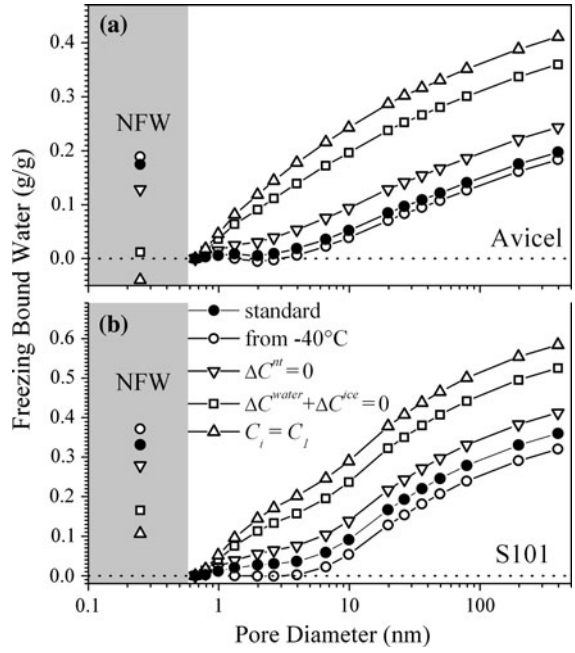

Fig. 8 Analyzed thermoporometry data from **a** Avicel and **b** S101, with contents of non-freezing water, NFW (g/g), shown in the gray areas. Data analysis with the standard method (*filled circles*) is compared to modified methods (*empty symbols*): (1) starting from data at −40 °C (*circles*), (2) neglecting ΔC^{nt} (*downward triangles*), (3) neglecting $\Delta C^{water} + \Delta C^{ice}$ (*squares*), and (4) neglecting all ΔC (implying $C_i = C_1$) (*upward triangles*). For definition of terms, see Eq. 5A–5D

for accurate TP-DSC. Moreover, NFW contents were also critically influenced by C_i corrections (see symbols in gray areas of Fig. 8).

Correlations between techniques

Cellulose characterization by DVS and TP-DSC provide many parameters that could reflect material properties. DVS equilibrium data, after application of the HH model, provides three parameters (m_0, ΔG_h and ΔG_d) from desorption, plus the corresponding three parameters from sorption. DVS kinetic data (considering only $h \leq 0.8$) provides eight parameters ($t_{1/16}$–$t_{1/8}$) from desorption plus the corresponding eight from sorption. TP-DSC provides fifteen heating steps with measurements of freezing bound water, plus the parameter NFW. Hence, these techniques jointly provide 38 parameters. It is beyond the scope of this work to investigate all possible relations within this data set. Nevertheless, a few correlations are presented with the aim of either understanding the phenomena behind the parameters, or verifying correlations that are expected based on simple interpretation of DVS and TP-DSC results. For each pair of parameters, the corresponding Pearson correlation coefficient r was calculated.

The first comparison is between sorption kinetic and equilibrium parameters. The characteristic time $t_{1/16}$–$t_{1/8}$ at $h = 0.4$ correlated positively ($r = 0.61$) with sorption m_0. These two parameters (previously presented in Figs. 4 and 7a, respectively) are plotted one against the other in Fig. 9. It is noteworthy that similar correlations ($r = 0.69$, 0.56, 0.58, and 0.66) were also observed at $h = 0.2$, 0.3, 0.5, and 0.6, respectively. These correlations suggest that, at intermediate relative humidities ($0.2 \leq h \leq 0.6$), the amount of monolayer water (m_0) plays a role in modulating sorption kinetics. This role, however, is limited, as suggested from data dispersion in Fig. 9, which is far beyond the magnitude of error bars (1σ precisions estimated from standard deviations in repeated measurements of selected samples). That is, additional, unknown material properties likely contribute to sorption characteristic times. In addition to these correlations at $0.2 \leq h \leq 0.6$, lower correlations ($r = 0.17$ and 0.30) with sorption m_0 were observed at $h = 0.1$ and 0.7, respectively, and a negative correlation ($r = -0.40$) was observed at $h = 0.8$.

The second comparison is between NFW determined by TP-DSC and m_0 derived from sorption isotherms. Both parameters estimate cellulose-water contact area: NFW is the non-freezing water layer, while m_0 is the molecular monolayer coverage. Hence, a positive correlation between them is expected. Moreover, both parameters are given in the same units (water mass per dry mass, g/g). Figure 10 shows NFW against sorption m_0. Each symbol is mean NFW

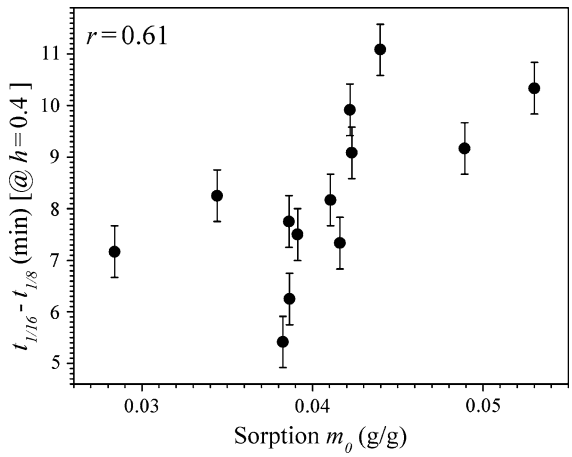

Fig. 9 Dynamic vapor sorption characteristic time ($t_{1/16}$–$t_{1/8}$) at relative humidity $h = 0.4$ versus monolayer water m_0 derived from equilibrium sorption isotherms. *Error bars* are estimated 1σ precisions. Correlation coefficient $r = 0.61$

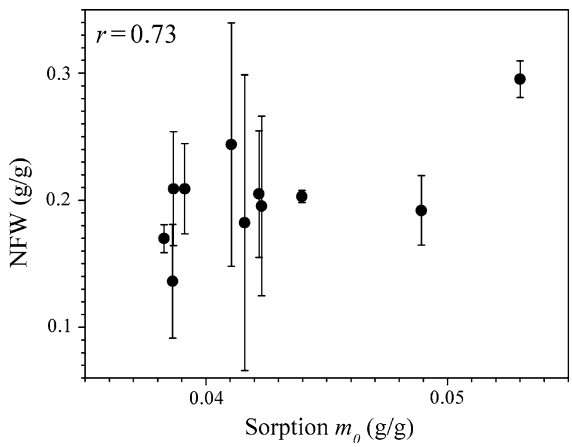

Fig. 10 Non-freezing water (NFW) measured by thermoporometry versus monolayer water m_0 measured by vapor sorption. *Symbols* are mean NFW (from repeated measurements) and *error bars* are standard deviations of mean NFW. Correlation coefficient $r = 0.73$

(from three or four repetitive TP-DSC measurements), and each error bar is the standard deviation of the mean, which estimates precision of mean NFW. Bacterial cellulose was removed from the data because its TP-DSC results presented poor repeatability. As expected, a positive correlation ($r = 0.73$) between NFW and m_0 was observed. One notes that the sizes of error bars represent the dispersion among data points, indicating that NFW precision is the main cause of data dispersion. In addition to this precision issue, NFW may also be inaccurate because its determination by TP-DSC is very sensitive to corrective terms (see Fig. 8). One concludes that both NFW and m_0 are valid measurements of cellulose-water contact area, but m_0 is much better because it is measured more precisely.

The third comparison is related to desorption-sorption hysteresis (see examples in Fig. 6). Hysteresis can result from capillary condensation or from inherited conformations. (Desorption inherits conformations from more swollen states, whereas sorption inherits from more collapsed states.) The rigid mesoporous silicas presented in Fig. 2 present sorption hysteresis only due to capillary condensation, because conformational changes are present only in swellable matrices (as celluloses). In either case (capillary condensation or inherited conformation), hysteresis is likely related to the suprafibrillar organization of cellulose, which also determines wet-state porosity. Hence, a positive correlation is expected between desorption-sorption hysteresis and porosity. This hypothesis is tested in Fig. 11, which correlates cumulative freezing bound water with the difference between desorption and sorption m_0. This difference (between filled and empty symbols in Fig. 7a) is taken to represent hysteresis. The inset of Fig. 11 presents the correlation coefficient r as a function of pore diameter. The correlation is maximum for pores up to 20 nm. Data from this pore diameter is shown in the major graph of Fig. 11. The appreciable correlation ($r = 0.82$) supports that desorption-sorption hysteresis and wet porosity are both derived from the underlying suprafibrillar cellulose organization. In addition, the correlation suggests that desorption m_0 counts, in addition to water monolayer, water trapped in pockets remaining from wet-state pores. Evaporation from these water pockets may explain the general characteristic time of desorption observed in Fig. 5.

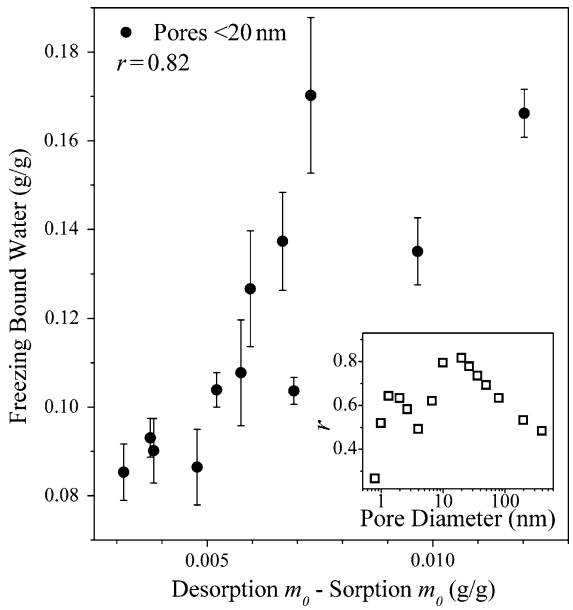

Fig. 11 Cumulative freezing bound water (pores up to 20 nm) versus the difference between desorption and sorption m_0. *Filled circles* are means (from repeated measurements) and *error bars* are standard deviations of the means. The *inset* presents the correlation coefficient r as a function of pore diameter. Maximum $r = 0.82$ was derived for pores <20 nm, whose data is shown in the main graph

Conclusion

This article detailed the application of dynamic vapor sorption and calorimetric thermoporometry to probe water in celluloses. Novel insights to these analytical techniques were derived from theoretical developments, experimental improvements, and analysis of model mesoporous materials. Analysis of a heterogeneous set of celluloses indicated the general and the material-specific analytical parameters. In particular, celluloses presented substantial variability in sorption kinetics, but material properties governing this kinetics are not clear. Nevertheless, new insights on the kinetics and hysteresis of vapor sorption were brought by exploring correlations between the analytical techniques. The presented developments and results will guide future application of dynamic vapor sorption and thermoporometry to probe water in celluloses.

Acknowledgments Research supported by FAPESP (project 2010/05523-3).

References

Brun M, Lallemand A, Quinson J-F, Eyraud C (1977) A new method for the simultaneous determination of the size and the shape of pores: the thermoporometry. Thermochim Acta 21:49–88

Burgert I, Fratzl P (2009) Plants control the properties and actuation of their organs through the orientation of cellulose fibrils in their cell walls. Integr Comp Biol 49:69–79

Dash JG, Rempel AW, Wettlaufer JS (2006) The physics of premelted ice and its geophysical consequences. Rev Mod Phys 78:695–741

Hailwood AJ, Horrobin S (1946) Absorption of water by polymers: analysis in terms of a simple model. Trans Faraday Soc 42:B084–B092

Hansen-Goos H, Wettlaufer JS (2010) Theory of ice premelting in porous media. Phys Rev E 81:031604

Henriksson G, Lennholm H (2009) Cellulose and carbohydrate chemistry. In: Ek M, Gellerstedt G, Henriksson G (eds) Wood chemistry and wood biotechnology. de Gruyter, Berlin, pp 71–100

Kocherbitov V, Ulvenlund S, Kober M, Jarring K, Arnebrant T (2008) Hydration of microcrystalline cellulose and milled cellulose studied by sorption calorimetry. J Phys Chem B 112:3728–3734

Kohler R, Alex R, Brielmann R, Ausperger B (2006) A new kinetic model for water sorption isotherms of cellulosic materials. Macromol Symp 244:89–96

Landry MR (2005) Thermoporometry by differential scanning calorimetry: experimental considerations and applications. Thermochim Acta 433:27–50

Lide DL (ed) (2006) CRC handbook of chemistry and physics, 87th edn. CRC Press, Boca Raton, p 6

Lowell S, Shields JE, Thomas MA, Thommes M (2010) Characterization of porous solids and powders: surface area, pore size and density. Springer, Dordrecht

Luukkonen P, Maloney T, Rantanen J, Paulapuro H, Yliruusi J (2001) Microcrystalline cellulose-water interaction—a novel approach using thermoporosimetry. Pharm Res 18: 1562–1569

Maloney TC, Paulapuro H, Stenius P (1998) Hydration and swelling of pulp fibers measured with differential scanning calorimetry. Nord Pulp Pap Res J 13:31–36

Mihranyan A, Llagostera AP, Karmhag R, Strømme M, Ek R (2004) Moisture sorption by cellulose powders of varying crystallinity. Int J Pharm 269:433–442

Park S, Venditti RA, Jameel H, Pawlak JJ (2006) Changes in pore size distribution during the drying of cellulose fibers as measured by differential scanning calorimetry. Carbohydr Polym 66:97–103

Petrov OV, Furó I (2009) NMR cryoporometry: principles, applications and potential. Prog Nucl Magn Reson Spectrosc 54:97–122

Skaar C (1988) Wood-water relations. Springer, Berlin

Stone JE, Scallan AM (1968) A structural model for the cell wall of water-swollen wood pulp fibres based on their accessibility to macromolecules. Cellulose Chem Tech 2:343–358

Xie Y, Hill CAS, Jalaludin Z, Sun D (2011) The water vapour sorption behaviour of three celluloses: analysis using parallel exponential kinetics and interpretation using the Kelvin-Voigt viscoelastic model. Cellulose 18:517–530